

See discussions, stats, and author profiles for this publication at: <https://www.researchgate.net/publication/255180421>

End-Coupling Reactions in Incompatible Polymer Blends: From Droplets to Complex Micelles through Interfacial Instability

ARTICLE *in* MACROMOLECULES · JUNE 2013

Impact Factor: 5.8 · DOI: 10.1021/ma400700n

CITATIONS

4

READS

1,099

2 AUTHORS:



Anatoly V Berezkin
Technische Universität München
30 PUBLICATIONS 173 CITATIONS

[SEE PROFILE](#)



Yaroslav V Kudryavtsev
Russian Academy of Sciences
62 PUBLICATIONS 354 CITATIONS

[SEE PROFILE](#)

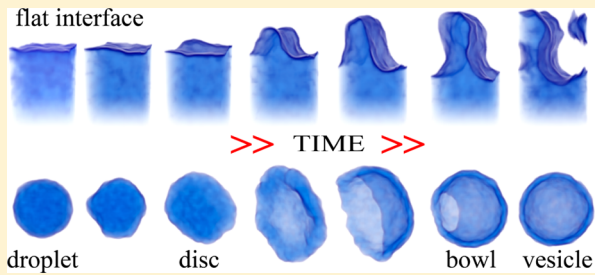
End-Coupling Reactions in Incompatible Polymer Blends: From Droplets to Complex Micelles through Interfacial Instability

Anatoly V. Berezkin[†] and Yaroslav V. Kudryavtsev^{‡,*}

[†]Max-Planck Institut für Eisenforschung GmbH, Max-Planck Strasse 1, 40237 Düsseldorf, Germany

[‡]Topchiev Institute of Petrochemical Synthesis, Russian Academy of Sciences, Leninsky prosp. 29, 119991 Moscow, Russia

ABSTRACT: Simulations by dissipative particle dynamics revealed a possibility to produce micelles of diverse morphologies via irreversible end-coupling reaction in polymer melts containing a particulate phase. It is demonstrated that the reaction at the surface of a polymer A droplet immersed in a melt of polymer B leads to the droplet instability and subsequent micelle formation. Depending on the length ratio of reacting chains and its own size, the droplet is either emulsified into a set of small micelles or converted into a single micelle, which can have rather complex internal structure. A morphology diagram containing structures that are typical for polymer solutions, in particular vesicles, bowls, worms, star-like and crew-cut micelles with multiple internal domains, is first presented for polymer melts. Investigation of the reaction kinetics reveals subsequent linear, saturation, and exponential autoacceleration regimes. By simulations and using simple scaling arguments, it is explained how the barrier properties of a diblock copolymer layer formed at the A/B interface depend on the copolymer composition and droplet curvature. It is found that the scenario of the instability development is much different for flat and spherical A/B interfaces.



INTRODUCTION

Controlled processing of polymer blends into composite materials is often hindered by phase separation of their components, most of which are incompatible due to the low entropy of mixing in polymers.¹ Reactive compatibilization is a strategy that aims to chemically bind immiscible polymers on a microscale thus increasing homogeneity of a composite and improving its macroscopic properties.^{2–5} In many cases, reactive melt blending facilitates emulsification providing a simple route toward nanodisperse polymer composites with enhanced processability, ductility, toughness, transparency, heat and creep resistance,^{6–8} as well as to novel nanoporous polymeric materials.^{9,10} For instance, an irreversible coupling between complementary reactive groups at chain ends or along their backbones produces linear or graft block copolymers that gradually change the structure and properties of the interphase, and, in turn, influence the kinetics.

Whereas it is successfully implemented in polymer engineering for decades,¹¹ the *in situ* copolymer formation under heterogeneous conditions remains a poorly explored area from the standpoint of fundamental science. Owing to the possibility of separating such factors as diffusion, reaction, accumulation of the reaction products, phase structure, etc., a flat interface between quiescent melts of two incompatible homopolymers is the most studied model system in theory,^{12–19} by simulations,^{20–27} and experimentally.^{19,28–40} These studies are focused on the reaction kinetics, i.e., how fast does the copolymer population grow at the interface, and on a spontaneous reaction-driven instability leading to the interface roughening and formation of diverse microstructures. Our

recent simulations by dissipative particle dynamics^{25–27} demonstrated that the instability develops similarly to the microphase separation in block copolymer melts and it can significantly accelerate end-coupling.

On the other hand, the interfacial instability was also reported^{41–43} for polymer blends that initially contain a particulate phase and react under mixing conditions. As far as we know, reactive coupling between polymers was never modeled in a system with spherical interface. Aimed at filling this gap, we report here on the coarse-grained molecular simulations that are performed for a droplet of one polymer immersed into the bulk of another polymer (the droplet-matrix model). The polymers are incompatible and functionalized at one end so that their coupling at the interface produces a diblock copolymer. The kinetics and structural rearrangements are monitored until one of the reactants is exhausted and their characteristics are compared to those of end-coupling at the initially flat interface.

As was shown experimentally⁴⁴ and supported by our simulations,²⁵ the interfacial reaction rate depends on the copolymer brush thickness, density, and conformation of blocks. Brush bending, which takes place at a curved interface, influences those parameters and one can expect that it alters the reaction kinetics as well. Our simulations give a quantitative account of this effect, which appears to be unexpectedly strong, in close agreement with simple scaling arguments.

Received: April 4, 2013

Revised: May 21, 2013

Published: June 4, 2013

The difference between end-coupling behavior at curved and flat interfaces also stems from the fact that the surface instability can at once affect the whole structure of a spherical particle, while this is impossible for a rather thick flat layer with only one reacting boundary. On that basis, it is natural to find more morphological diversity in microstructures that can evolve from the droplet after it loses stability in the course of the coupling reaction. It is shown below that such hypothesis is true and a wide variety of micelles, including vesicles (polymersomes), worms, bowls, and internally structured crew-cut aggregates, can appear in a melt if the longer polymer is initially confined within the particulate phase. Our findings are discussed in light of experimentally observable microstructures.

■ MODEL AND SIMULATION TECHNIQUE

We use a coarse-grained molecular dynamics technique referred to as dissipative particle dynamics (DPD), which was proposed by Hoogerbrugge and Koelman^{45,46} for the simulation of liquid suspensions and extended to polymer systems by Espanol, Groot, and Warren.^{47,48} DPD particles represent large groups of atoms and interact through short-ranged soft repulsive potentials. Polymer chains are formed by connecting the particles with Hookean springs of zero equilibrium length and the spring constant $K = 4$. Particle size is assumed to exceed the Kuhn segment length so that the modeled polymer is fully flexible.⁴⁹ It is worth mentioning that the DPD technique appeared very suitable in modeling the formation of standard^{49,50} and more exotic^{51–55} microstructures in the block copolymer systems.

Detailed description of the model and a brief review of applying DPD to reacting polymer systems can be found in our previous papers.^{25–27} As recommended in refs 47 and 48, we take the average density of particles $\rho_0 = 3$, noise amplitude of the random force $\sigma = 3$, and amplitude of the conservative repulsive force between similar particles $a_{ii} = 25$. The repulsion parameter for dissimilar particles a_{ij} is related to the interaction parameter χ of the Flory–Huggins theory as⁴⁸

$$a_{ij} = \chi / 0.306 + 25 \quad (1)$$

In our simulations of immiscible melts A and B, the typical value is $a_{AB} = 50$ so that if a diblock copolymer of $N \sim 10$ segments is formed it enters the strong segregation regime⁵⁶ with $\chi N \sim 10^2$, when blocks are rather incompatible and the copolymer is accumulated at the A/B interface. The equations of particle motion were solved using the so-called DPD-VV integration scheme⁵⁷ (modified velocity–Verlet algorithm) with the time step $\delta t = 0.04$. *Chemical reactions* were modeled using a probabilistic approach,²⁵ which is actively implemented in MD,^{58,59} DPD,^{60,61} and Monte Carlo⁶² simulations of polymerization and polycondensation.

Two functionalized particles can react (and become connected) at a short distance only, which is called the reaction radius r_R (here $r_R = 1$ as well as the cutoff radius for all nonbonded DPD interactions.⁴⁷) Reaction in every pair of particles proceeds with a certain predefined probability p_0 , which is chosen to be small enough so that the reaction controlled short-time kinetics, typically observed in experimental studies of end-coupling, is reproduced. In our simulations, the reaction takes place every 10th time step with the probability $p_0 = 0.01$ yielding the reaction probability per unit time $p_R = p_0 / (10\delta t) = 0.025$, which provides a good

balance between the computational efficiency and realistic end-coupling kinetics.

The relation between DPD time and real time can be roughly estimated by calculating the average lifetime of a reactive group in the homogeneous reacting blend. For a bimolecular reaction, it reads $\tau_h = 1/(kc_i)$, where k is the reaction rate constant, and c_i is the initial concentration of limiting functional groups. In the typical reactive blending process (aliphatic amine and anhydride attached to PMMA chain ends, $T = 180$ °C³²), $k \approx 10^2$ kg/(mol·min) and $c_i \approx 0.0035$ mol/kg so that $\tau_h \approx 1.7 \times 10^2$ s. For the DPD model at $N_A = N_B$ one finds $k \approx 4\pi p_R/3$, $c_i = \rho_0 / N_A = 3 / N_A$ that yields $\tau_h \approx N_A / (4\pi p_R) = 19.1$ at the typical simulation parameters $N_A = 6$, $p_R = 0.025$. Thus, for the numerical values used the DPD time unit corresponds to 8.9 s of real time and in general, it can vary from fractions to tens of seconds. More detailed discussion on comparing characteristic reaction and diffusion time scales and mapping the simulated kinetics onto the real-time scale can be found in ref 25.

Simulation box of the size $l_x \times l_y \times l_z = (64 r_c)^3$ (about 786400 particles) with periodic boundary conditions initially contained immiscible melted polymers A and B. A spherical droplet of the polymer A was surrounded by the polymer B matrix as illustrated in Figure 1. The droplet radius R was varied from 4

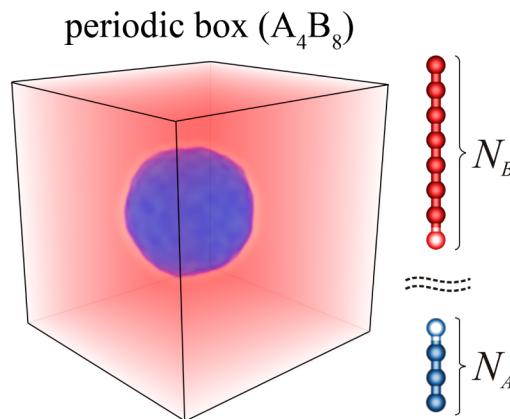


Figure 1. Structure of the initial droplet-matrix system A_4B_8 ($N_A = 4$, $N_B = 8$, the droplet radius $R = 16$). Reactive units A and B containing complementary functional groups are highlighted.

to $16 r_c$ so that its diameter was at least two times smaller than the box size for preventing influence of mirrored droplet images on the kinetics. Functionalized chain ends A and B (one per chain) could irreversible react forming a diblock copolymer AB.

Simulated systems were denoted as $A_{N_A}B_{N_B}$. In order to elucidate the role of copolymer composition, reactant lengths N_A and N_B were varied. In the most of the simulations, the overall copolymer length $N = N_A + N_B$ was fixed at 12 thus producing a line of models A_2B_{10} , A_3B_9 , ..., A_6B_6 , ..., A_9B_3 , $A_{10}B_2$. Additional simulations were carried out for A_2B_2 , A_4B_2 , and $A_{22}B_2$ systems, in which crew-cut micelles with short outer B blocks were observed. All the systems were characterized by the same degree of incompatibility $\chi N = 91.8$ by adjusting the repulsion parameter a_{ij} in eq 1.

After an initial relaxation for 10^5 steps, the end-coupling was turned on and simulations were carried out up to 1.5×10^6 steps (6×10^4 dimensionless time units). At the selected reaction probability, this time was long enough to consume all reactive A groups so that in the final state the melts contained copolymer AB chains and unreacted B chains.

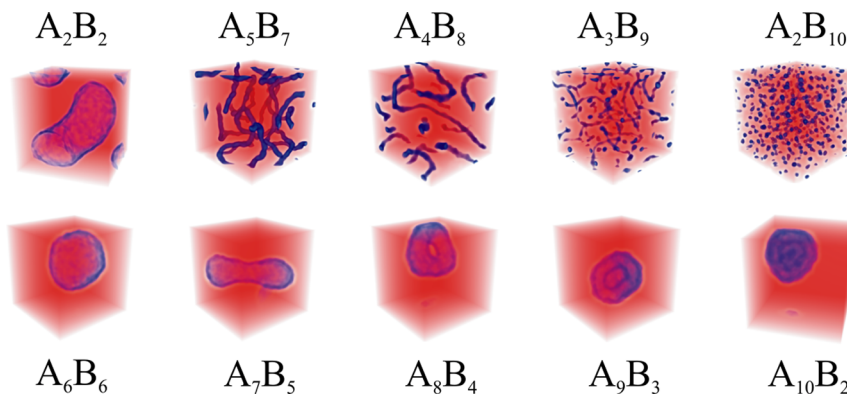


Figure 2. Final morphologies for different lengths of the reacting (red) A and (blue) B polymers in the droplet-matrix model. Radius of the initial droplet A is fixed at $R = 16$.

In every system, the kinetics was averaged over eight independent runs started from different initial configurations.

RESULTS AND DISCUSSION

General Trends. Our previous studies^{25–27} gave a clear picture of the reactive compatibilization by end-coupling of melted immiscible polymers in the flat bilayer model. The standard scenario begins with a linear growth of the copolymer coverage n (the number of copolymer chains per unit area of the initial interface) at a nearly free interface, according to the second-order reaction kinetics. It is followed by saturation due to the formation of a copolymer brush or, in some cases, of a layer depleted in reactants. When the value of n gets close to that in the microdomain structure of a corresponding pure diblock copolymer, the interface becomes unstable and rough thus triggering emulsification of the blend. At that moment the kinetics can be substantially accelerated, particularly, if both phases keep continuity. Further couplings lead to a microstructure build-up on the scale of a whole system, followed by a slow process of local ordering.

Evolution of the droplet-matrix model investigated in this study gives rise to much more diverse and complex morphologies, as is illustrated in Figure 2. It is clearly seen that the initial droplets containing a shorter reactant (A_5B_7 , A_4B_8 , A_3B_9 , A_2B_{10}) are unstable and subjected to emulsification in the course of the reaction. In the final state, spherical (A_2B_{10}), necklace-like (A_3B_9), or cylindrical (A_5B_7 , A_4B_8) micelles of the diblock copolymer AB are uniformly distributed in the bulk of remaining polymer B. Each micelle has a core of A blocks and a stabilizing corona of B blocks.

For the other initial systems, with the reactants of equal length (A_2B_2 and A_6B_6) or longer chains inside the initial droplet (A_7B_5 , A_8B_4 , A_9B_3 , $A_{10}B_2$), a single micelle is observed in the course of the reaction. In all the cases, it has a vesicular structure with walls made of A units and B units inside and outside. Large vesicles are filled with unreacted B chains. The micelle shape becomes more complex with decreasing the maximum possible coverage value $n_{\max} = \rho_0 R / (3N_A)$, which is attained at full conversion of the polymer A. At $R = \text{const}$ (Figure 2), by increasing N_A one gets spherical vesicles (A_2B_2 and A_6B_6), hollow cylinders (A_7B_5), tori (A_8B_4), and multi-compartment structures (A_9B_3 and $A_{10}B_2$).

Full kinetic curves for the model systems with the fixed total copolymer length $N_A + N_B = 12$ and droplet radius $R = 16$ are plotted in Figure 3. On the whole, the smaller N_A/N_B , the easier is the emulsification of the initial droplet, and the faster is

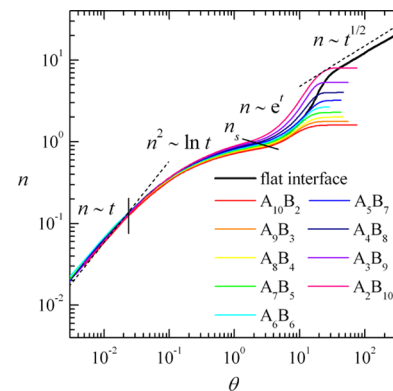


Figure 3. Time dependences of the interfacial copolymer coverage n for end-coupling in droplets with different N_A/N_B ratio and fixed total length $N_A + N_B = 12$ and radius $R = 16$. The black solid line describes the reaction at the initially flat interface at $N_A = N_B = 6$, for which case the different kinetic regimes are shown.

the kinetics. Comparing the color curves with the black one obtained by us in refs 25 and 27 for the reacting A_6B_6 flat bilayer system, we may conclude that at least three first regimes (linear, saturation, and acceleration, as discussed below) are qualitatively reproduced for the reaction at a spherical interface. The terminal diffusion controlled regime was not accessible because of the insufficient size of A droplets.

Below we consider in more detail kinetical and morphological differences between various droplet-matrix and flat bilayer model systems.

Early Stages. At the earliest stage the reaction rate is proportional to the concentrations of functional groups in contacting melts. Neglecting depletion of the reactants and buildup of the reaction product, one gets a linear dependence of the interfacial coverage n on time:

$$\frac{dn}{dt} = k_0 \rho_A^0 \rho_B^0 = k_0 \frac{\rho_0^2}{N_A N_B} \approx \text{const}, \quad n(t) = K\theta, \\ K = \text{const}, \quad \theta = \frac{tp_R}{N_A N_B} \quad (2)$$

Here k_0 is the rate constant ($k_0 \sim p_R$), ρ_A^0 and ρ_B^0 are the initial bulk densities of reactive units. The dimensionless time θ is introduced to get a universal master curve $n(\theta)$ describing the kinetics independently of architecture and composition of a reacting system, as well as of the reaction probability p_R . Our

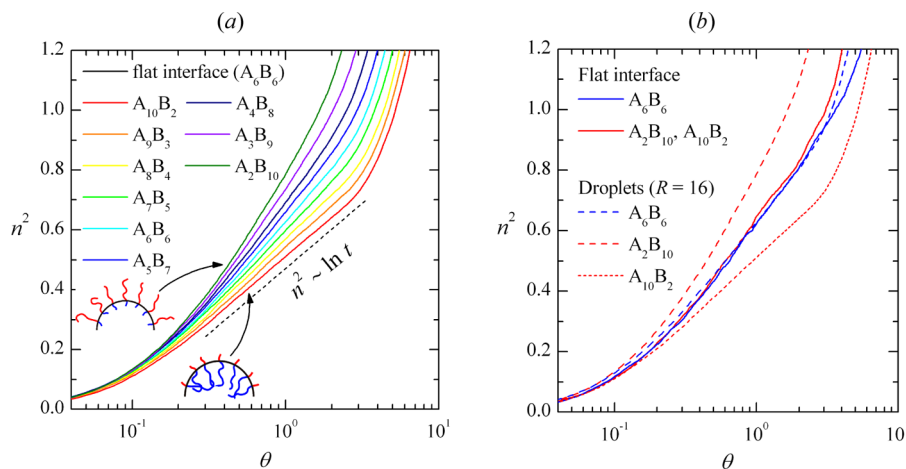


Figure 4. (a) Saturated regime of the end-coupling for A droplets covered by AB copolymers of different composition (shown) and fixed radius $R = 16$. (b) Comparison of the kinetics for droplet-matrix and flat bilayer systems.

previous analysis²⁷ revealed that the effective coupling rate K is slightly dependent on polymer lengths and positions of functionalized groups in the chains but at the earliest stage those effects are negligible. As is seen from Figure 3, the reaction controlled regime described by the linear kinetics is well reproduced for the droplet-matrix systems studied in this work.

At $\theta \approx 0.02$, the interface is still unperturbed but the reaction rate begins to decrease due to the screening effect of a copolymer brush formed at the interface (diffusion control effects are neither expected¹⁷ nor observed⁴ in fully functionalized polymer melts, the Rouse time for any initial system in this study being of the order of $\theta \approx 0.01$). The kinetic curves drift apart and simultaneously diverge from linearity, which is shown in more detail in Figure 4a. In all the cases, the saturation regime $n \sim (\ln t)^{1/2}$ is gradually established, similarly to flat bilayer systems,^{25–27} but with the difference that the proportionality constant for the droplet-matrix model depends not only on the total copolymer length $N_A + N_B$ but also on the polymer length ratio N_A/N_B . At a flat interface, it does not matter on which side the longer blocks are situated and at fixed $N_A + N_B$ the same kinetics is observed (Figure 4b). If, however, a brush is formed at a curved interface, its convex side is effectively rarefied, whereas the concave one is thickened. As a result, when chains in the particle are longer than that in the bulk, the reaction proceeds considerably slower comparing to the flat bilayer model, and faster in the opposite case. Symmetric systems ($N_A = N_B$) demonstrate nearly the same kinetics, which is only slightly slower for the droplet-matrix model.

The role of droplet size R is illustrated by Figure 5. For smaller droplets, the reaction rate is increased at $N_A < N_B$ and decreased at $N_A \geq N_B$ provided that $N_A + N_B$ is fixed. In the first case, longer B blocks get more freedom outside the droplet, whereas in the second situation longer A blocks are more confined inside it. The retardation is more pronounced than acceleration, especially, if the droplet radius becomes comparable to the brush thickness, in which case the conversion is considerably lower and even the logarithmic trend does not hold (see the dotted green curve). Thus, the permeability of a droplet interior appears to be the key factor of reactive compatibilization in melt emulsions and it can be

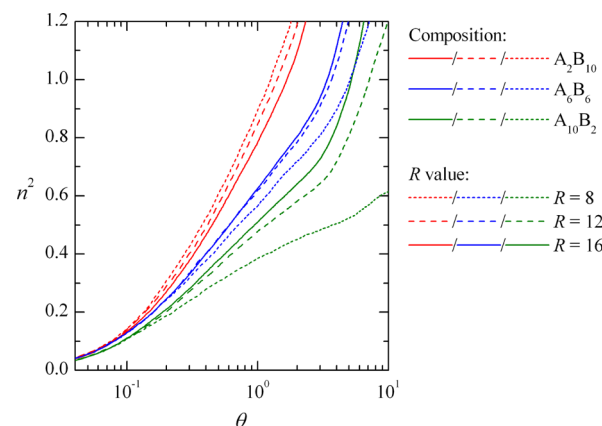


Figure 5. Saturation regime in the droplets of different size and composition (shown).

effectively regulated by the proper choice of reactant lengths and fineness of a mixture.

Main characteristics of the saturation regime revealed by simulations can be captured by a simple scaling approach, which was originally proposed in refs 14–16 for the flat bilayer model. Unlike the linear regime, the apparent rate constant should depend on the copolymer coverage n thus reflecting the fact that the interfacial concentrations of A and B ends are lower than their bulk values.

As shown in Appendix A, the kinetics of interfacial end-coupling at the saturation regime is asymptotically described by the relation

$$\frac{F_{el}(n(t))}{k_B T} = \ln\left(\frac{k_0 \rho_A^0 \rho_B^0}{n_{cr}} t\right) \quad (3)$$

which becomes valid at $n \gg n_{cr}$, where $n_{cr} \approx (N_A + N_B)^{-1/2} \rho_0 a^{-2}$ is the critical coverage separating linear and saturation regimes (at $n = n_{cr}$ copolymer blocks at least on one side of the brush start to feel one another and therefore begin to stretch) and a is the monomer unit size assumed to be the same for A and B units. The function $F_{el}(n)$ describes the free energy barrier due to the copolymer brush formation. It reads

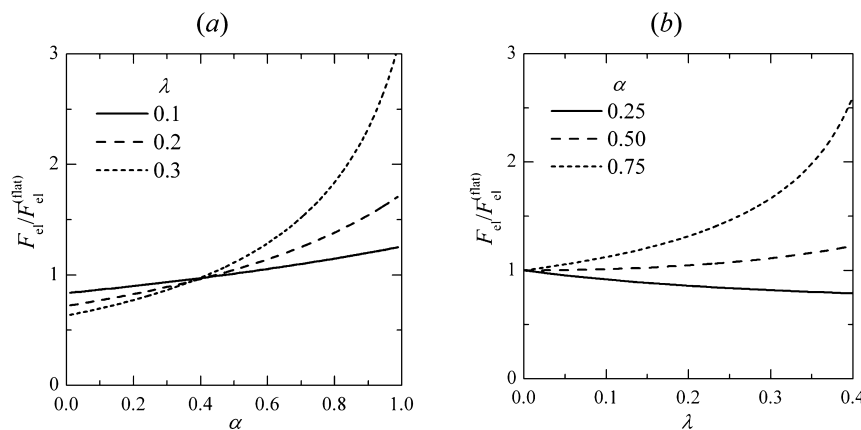


Figure 6. Energy barrier for end-coupling at the spherical interface (relative to the flat interface at a same copolymer coverage) vs (a) α at different λ and (b) λ at different α .

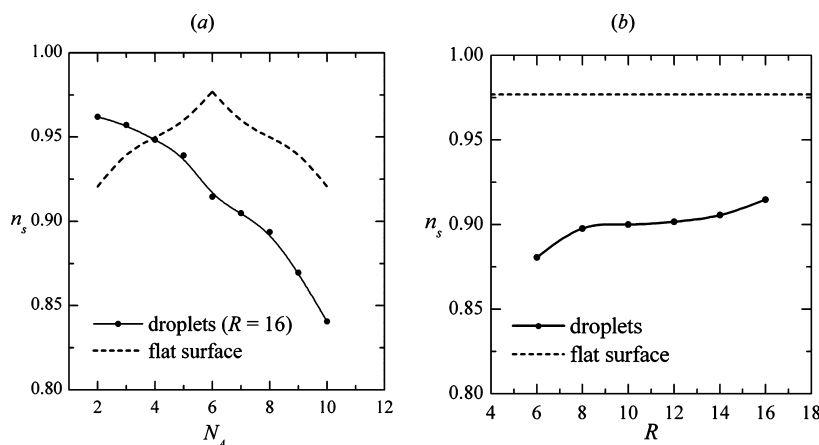


Figure 7. Saturation copolymer coverage n_s as the function of the (a) copolymer composition at fixed $R = 16$ and $N_A + N_B = 12$ and (b) droplet size R for the symmetric copolymer A_6B_6 . Corresponding dependences for the flat bilayer model are shown by dashed lines.

$$F_{\text{el}}(n) = F_{\text{el}}^{(\text{flat})}(n) \frac{9}{\lambda^2(n)} \left(\frac{(1 + (\alpha\lambda(n) - 1)^{1/3})^2}{\alpha} + \frac{(1 - (1 + (1 - \alpha)\lambda(n))^{1/3})^2}{1 - \alpha} \right) \quad (4)$$

where $\alpha = N_A/(N_A + N_B)$ describes the copolymer asymmetry, $\lambda = 3n(N_A + N_B)\alpha^3/(\rho_0 R)$ is the brush to droplet volume ratio, which is directly proportional to the copolymer coverage n and inversely to the droplet radius R , and $F_{\text{el}}^{(\text{flat})}(n)/(k_B T) = 3n^2(N_A + N_B)a^4/(2\rho_0^2)$ is the energy barrier for meeting A and B end groups at a flat interface ($\lambda \rightarrow \infty$).

For a flat interface, $F_{\text{el}} = F_{\text{el}}^{(\text{flat})} \sim n^2$ so that $n \sim (\ln t)^{1/2}$, as was predicted in refs 15 and 16. The curvature effect can be understood by comparing F_{el} with $F_{\text{el}}^{(\text{flat})}$ for different values of the parameters α and λ . As is seen from Figure 6a, long chains within the droplet (large α) considerably increase the barrier, whereas short chains (small α) have the opposite effect, which is, however, much less pronounced. The same kinetic trends are observed in simulations, as is shown in Figures 4 and 5. For $\alpha \approx 0.4$ ($N_A \approx 2N_B/3$), the barriers at the flat and spherical interfaces are nearly the same, being dependent only on the copolymer coverage n and almost independent of the droplet radius R .

Symmetric diblocks ($N_A = N_B$) form a brush, which is only slightly less penetrable at a curved interface compared to a flat

one (Figure 6b). For small λ (a big droplet) it can be demonstrated by expanding eq 4 in powers of $\lambda \sim 1/R$ (this expression was first derived in ref 63):

$$F_{\text{el}} = F_{\text{el}}^{(\text{flat})} \left(1 + \frac{4}{3} \left(\alpha - \frac{1}{2} \right) \lambda + \frac{13}{9} \left(\alpha^2 - \alpha + \frac{1}{3} \right) \lambda^2 + O(\lambda^3) \right) \quad (5)$$

It is seen that at $\alpha = 1/2$ the term proportional to λ drops out so that $F_{\text{el}}/F_{\text{el}}^{(\text{flat})} \approx 1 + (13/108)\lambda^2 = 1 + O(R^{-2})$ is always, yet only slightly, larger than unity (see the dashed curve in Figure 6b). This result explains closeness of the corresponding kinetic curves in Figure 4.

In the leading order eq 5 yields $F_{\text{el}} \approx F_{\text{el}}^{(\text{flat})} \sim n^2$ so that the saturation regime kinetics for big droplets should also obey the law $n \sim (\ln t)^{1/2}$, which is in fact observed in Figures 4, 5 for all the curves corresponding to $R = 16$. If R is decreased, eq 5 should be replaced with eq 4, which leads to more complex kinetic laws $n(t)$ that are nonlinear in the coordinates of Figures 4, 5.

Qualitative agreement between the simulation data and estimations by the scaling theory is evident but a quantitative fitting of the saturation regime could hardly be justified in view of the oversimplified theoretical model and relatively short chains studied by simulations.

Interfacial Instability. As was demonstrated before,^{25–27} a copolymer brush can considerably suppress interfacial end-coupling but cannot stop it completely. At a certain “saturation” time t_s (though it can be practically inaccessible for long chains³⁴) the interface becomes unstable. The droplet loses its spherical shape either by formation of “viscous fingers” and emitting small micelles or by global deformation, depending on the copolymer composition and droplet size. This leads to a dramatic growth of the interfacial area and acceleration of the reaction. At $t = t_s$ each kinetic curve in Figure 5 has a more or less visible upward inflection point, which marks the end of the saturation regime. The simulations revealed^{25–27} that the saturation coverage $n_s = n(t_s)$ is proportional to the equilibrium interfacial density of chains, c_∞ , in the melt of a diblock copolymer, which is formed in the reacting system at 100% conversion.

Dependences of the saturation coverage n_s on the copolymer composition and initial droplet size are shown in Figure 7, parts a and b, respectively. Generally speaking, n_s characterizes affinity of a copolymer brush to the interface where it is formed. As is seen from Figure 7a, the spherical interface most readily hosts asymmetric copolymers with the shortest inner block, whereas a maximum coverage at the flat interface is attained with symmetric diblocks. For a droplet of given size, there exists a block ratio N_A/N_B (for $R = 16$, $N_A/N_B = 1/2$), at which a unit area of the flat and spherical interfaces can accommodate the same number of diblocks. At larger N_A/N_B , the capacity of the flat interface is higher since placing long blocks in the droplet is disadvantageous, as was discussed above.

As follows from Figure 7b, symmetric copolymers form a denser brush at the flat interface than at the spherical one, and in the latter case n_s slowly grows with R . It agrees with the theoretical result that bending always leads to an increase, though slight, in the free energy of a symmetric diblock copolymer brush.

Late Stage Kinetics. Instability of the initial interface due to its overcrowding with the copolymer product distorts and roughens the interface thus launching major morphological changes in the blend. The interfacial area grows thereby increasing the reaction rate. In the flat bilayer model, most effectively emulsified are nearly symmetric systems, which exhibit exponential kinetics when a lamellar microstructure is being formed.²⁵ Instability in asymmetric systems develops much slower via continuous emission of micelles from the interface.²⁷

Simulations of relatively small droplets ($8 \leq R \leq 16$) reveal an existence of the autoacceleration regime $n \sim \exp t$ in all cases, independently of the resulting copolymer composition (Figure 8). As is seen from Figure 2, at $N_A < N_B$ droplets are emulsified into smaller micelles, whereas at $N_A \geq N_B$ they turn into vesicles. Variations in the duration of the acceleration regime are explained by decreasing the number of reacting end groups A with growing N_A .

Another interesting feature, which is readily seen at Figure 8, is that the exponential kinetics in all droplets is established much faster than in the symmetric flat bilayer. The reason becomes clear after we look at Figure 9 with snapshots illustrating the interface evolution for the same system A_6B_6 in the flat bilayer and droplet-matrix models. In the first case, a spherical protrusion grows on the initially flat interface then forming a new flat lamella. In the droplet-matrix model, an initially spherical domain A flattens and then turns into a vesicle by encapsulating a portion of the polymer B. It is evident that in

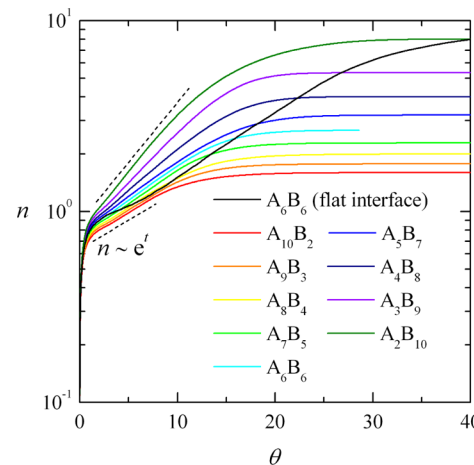


Figure 8. Reaction kinetics at the late stages of end-coupling for the droplet-matrix systems with different N_A/N_B ratio at $N_A + N_B = 12$ and $R = 16$. The black curve corresponds to the symmetric system with $N_A = N_B = 6$ in the flat bilayer model.

the first system the interfacial block copolymer layer is locally deformed to a much higher extent. Bending of the copolymer brush suppresses end-coupling at a considerable part of the interface. That is why, after finishing the saturation regime with nearly the same conversion (Figure 4b), the flat bilayer model starts to fall behind the droplet-matrix one during the instability development.

In all the cases, the acceleration regime is followed by retardation. In the bilayer systems studied in refs 25–27, this indicates a crossover to the terminal regime, in which the compatibilization is controlled by the diffusion of reagents within well-defined microdomains. Oppositely, in the droplets modeled in this work the reaction just stops because of the polymer A exhaustion.

Micelle Formation. Simulations of end-coupling in the droplet-matrix model yield a plethora of microstructures, some of which are shown in Figure 2. It makes sense to somehow arrange them by relating to structural parameters of the studied systems. Figure 10 represents our attempt to reduce the results to a diagram with coordinates copolymer coverage n – copolymer composition $N_A/(N_A + N_B)$. All initial systems start from the abscissa axis ($n = 0$) and move with conversion vertically up to the maximum coverage $n_{\max} = \rho_0 R / (3N_A)$, for which the final morphologies and their cross sections (where appropriate) are shown.

By varying the initial droplet radius R in the range from 6 to 16 at the fixed total macromonomer length $N_A + N_B = 12$, we found that the sequence of transformations observed in Figure 10 does not depend on R , though the domain boundaries, which are shown by the dashed lines, are shifted up to $\pm 50\%$ and notably fluctuate for the transient morphologies such as bowls. As a rule, structural transitions in smaller droplets take place at lower coverage n . For example, if R decreases from 16 to 6, then the borderline for the transition from sphere to disc at $N_A \geq N_B$ shifts down for about 15%. Thus, Figure 10, representing the case $R = 16$ and $N_A + N_B = 12$ gives also a qualitative picture of morphological changes in other simulated systems.

The left part ($N_A < N_B$) of the morphology diagram represents a homogeneous dispersion of star-like spherical or cylindrical A micelles in the bulk B. Since each melt contains excessive unreacted B polymers, its final morphology differs

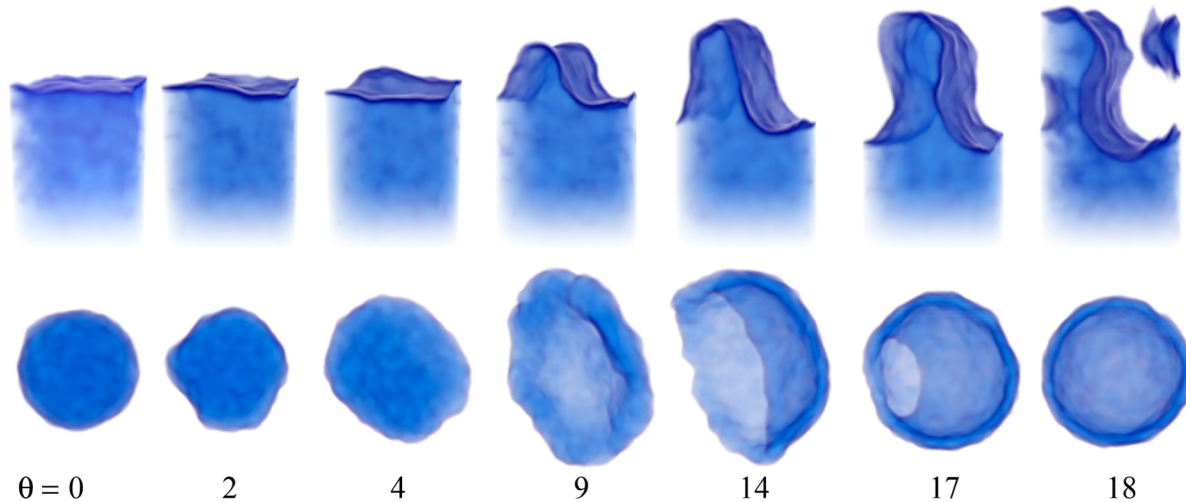


Figure 9. Development of the interfacial instability due to end-coupling reactions in the (upper row) flat bilayer and (bottom row) droplet-matrix systems A_6B_6 . The dimensionless time θ is defined by eq 2. The initial droplet radius $R = 16$. Only component A is shown.

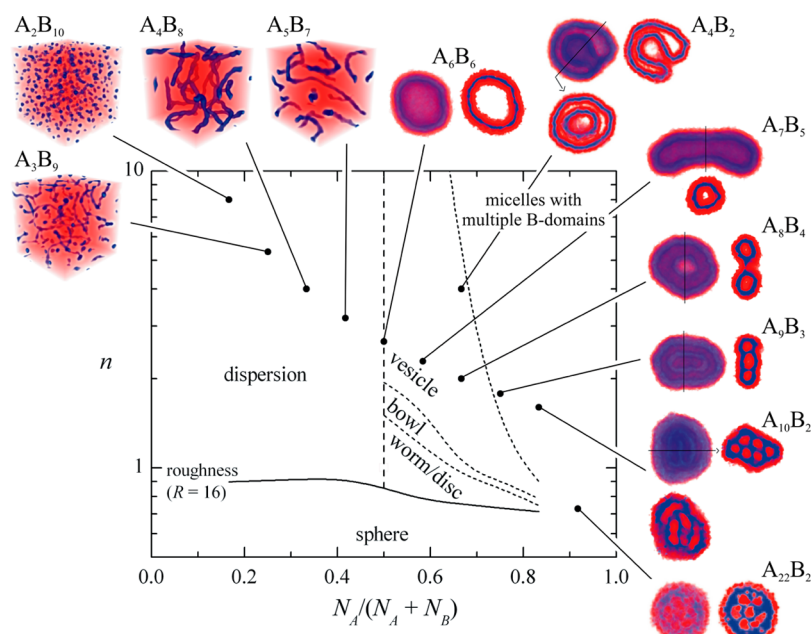


Figure 10. Morphology diagram for the droplet-matrix model in the coordinates copolymer coverage – copolymer composition. Final structures are shown in snapshots, where A and B particles are blue and red, respectively. For $N_A \geq N_B$, cross sections of the systems (frontal ones, if a cutting plane is not shown) are presented, with only copolymers visible. Solid curve corresponds to the saturation coverage $n = n_s$, at which the initial droplet with $R = 16$ becomes unstable. $\chi N = 91.8$.

from what is expected from the phase diagram of a pure AB copolymer melt.⁴⁹ For example, in the system A_2B_{10} micelles are observed instead of hexagonally packed cylinders, and in A_4B_8 and A_5B_7 there are cylinders rather than double-gyroid and lamellar morphologies, respectively.

At $N_A \geq N_B$ the diagram in Figure 10 contains a diversity of structures that look like a single object from outside but can have a rather complex interior. In the course of the reaction those structures evolve similar to what is depicted in the lower row of Figure 9. First of all, a droplet transforms from sphere to disc (sometimes through a worm-like micelle), which becomes bigger and thinner. Since chains are consumed at flat faces faster than at rounded edges, the disc takes a blood-cell-like shape (see the snapshot at $\theta = 9$) and then turns to a vesicle through a bowl-like structure. In larger droplets and for strongly

asymmetric copolymers such cycle can be repeated several times thus making an internal structure of the vesicle more and more complex (as in the systems A_4B_2 and $A_{22}B_2$ in Figure 10).

Nearly symmetric systems (A_6B_6) form simple spherical vesicles (polymersomes), whereas more asymmetric ones elongate (A_7B_5), then get a multicompartiment internal structure (A_8B_4), form multiple ordered B domains with an onion-like cross-section (A_4B_2 and A_9B_3) and, ultimately, small cylindrical ($A_{10}B_2$) or spherical ($A_{22}B_2$) B micelles in the bulk A all confined in a large spherical crew-cut micelle.

It is seen that all “classical” solution morphologies of copolymeric amphiphiles⁶⁴ are present in Figure 10, including intensively studied polymersomes^{65,66} that already have a record of practical applications⁶⁷ and less common worms⁶⁸ and bowls,⁶⁹ with the only exception for the cylindrical micelles

with Y-shaped junctions⁷⁰ (an analogue of the gyroid phase in block copolymer melts), presumably, due to a narrow interval of compositions, where they appear, and relatively small aggregation numbers. Ring-shaped cylinders (A_8B_4)⁷¹, onion-like structures (A_4B_2)⁷² and inverted multidomain micelles ($A_{10}B_2$ and $A_{22}B_2$)⁷³ were also experimentally observed in polymer solutions. Fragmentary data on the formation of complex morphologies were reported also for multicomponent polymer melts, in particular, worm-like micelles, vesicles, and onion-like structures were observed in PS-*b*-PB/PS blends,⁷⁴ vesicles, onion-like, and cucumber-like (similar to our $A_{22}B_2$ system) structures were found in PA-*b*-PIP-*b*-PS/PA blends.⁶

Our simulations demonstrate for the first time that all these morphologies can be formed in the simple model melt of diblock copolymer AB and homopolymer B. Such route does not require using selective solvents and could be useful for preparing novel polymeric nanomaterials of well-defined structure.

CONCLUSIONS AND OUTLOOK

In this study, the DPD modeling technique was used to simulate *in situ* irreversible end-coupling at the surface of a spherical droplet of polymer A immersed in the bulk of polymer B. It was studied in detail how the surface curvature and chain length ratio influence the reaction kinetics and various micellar microstructures that appear after the droplet becomes unstable. Though the same kinetic laws, as for the flat bilayer model studied in our previous papers,^{25–27} were detected, i.e., the linear, saturation, and acceleration regimes, it was found that the reactive compatibilization in the droplet-matrix model proceeds in a significantly different way.

Contrary to the flat bilayer model, N_A/N_B ratio plays a crucial role at the saturation regime. Specifically, long A chains placed into the droplet and converted to the copolymer blocks A by end-coupling create a thick brush at the surface, which considerably slows down the reaction. The influence becomes very strong when the droplet size is comparable to the length of an A block. The surface curvature effect is almost imperceptible at $N_A \approx 2N_B/3$ in the wide range of R values and is very weak (retardation) at $N_A = N_B$. After the initial droplet gets unstable and the reaction reaccelerates, all droplet-matrix systems demonstrate the exponential kinetics irrespectively of N_A/N_B , unlike the flat bilayer model, where the dependence $n \sim \exp t$ is predicted only for nearly symmetric systems.

The scenario of developing the instability at the initial A/B interface is also much different for the flat bilayer and droplet-matrix models. In the former case, there is a continuous process of emitting micelles, while the droplet is either emulsified into small micelles or deformed as a whole then being transformed into a vesicle or crew-cut micelle. Possible microstructures are schematized in the morphology diagram, which has many parallels to the structures that were observed experimentally in polymer solutions and block copolymer/homopolymer melt blends.

Our simulations demonstrated that it is worth thinking of reactive compatibilization for the controlled synthesis of micelles in droplet-matrix polymer melts. Its practical realization is hardly possible with the standard techniques for reactive blending, which do not provide strict control over the size and interaction of droplets. However, rapidly developing microfluidic devices seem attractive for solving the problems of colloidal stability during the micelle synthesis.⁷⁵ Interestingly, a similar idea of fabricating vesicles from a melt of premade

diblock copolymer AB and homopolymer C was put forward⁷⁶ as early as in 1997 but its verification by computer simulations at that time was problematic.

Moreover, reactive compatibilization could be applied to polymer solutions as well. Indeed, one of the experimental methods for obtaining amphiphilic block copolymer micelles from solutions is based on the evaporation of an immiscible organic solvent emulsified in water, which leads to increasing polymer concentration in the solvent droplets, lowering the interfacial tension, and causing the droplet instability.^{77,78} Another strategy utilizes controlled radical polymerization of a hydrophobic block in a monomer-in-water emulsion so that no organic solvent is required and the resulting concentration of micelles is higher.^{79,80} Our approach in a sense combines those ideas by exploiting chemical reactions to concentrate copolymer at the interface between immiscible liquids. Unfortunately, technical limitations do not allow us to perform DPD simulations in dilute solutions of reacting polymers but this task can be much easily attacked in experiments.

APPENDIX

Here we apply the simplified scaling approach of refs 14–16 for deriving eq 3 that describes the dependence of the interfacial copolymer coverage n on time at the saturation regime of end-coupling at the surface of a polymer A droplet situated in the bulk of polymer B.

Following ref 14 we can write:

$$\frac{dn}{dt} = k_0 \rho_{Ai} \rho_{Bi} \quad (A.1)$$

where ρ_{Ai} and ρ_{Bi} are the interfacial concentrations of A and B ends.

Being interested in the asymptotic saturation behavior, we assume that the copolymer brush with layer A of width L_A and layer B of width L_B constitutes a high potential barrier (exceeding $k_B T$) for unreacted A and B polymers, which have to penetrate the brush so that their end groups could meet at the interface. This leads to an exponential decrease in the concentrations

$$\rho_{Ai} = \rho_A^0 \exp(-F_A/k_B T), \quad \rho_{Bi} = \rho_B^0 \exp(-F_B/k_B T) \quad (A.2)$$

where F_A and F_B are the free energy penalties for embedding A and B chains into the brush. Note that the initial end concentrations ρ_A^0, ρ_B^0 are used instead their current bulk values because the total conversion remains small as long as the reaction proceeds at the initial interface only.

In strongly segregated systems, the main contribution to $F_A + F_B$ is due to chain stretching. In its simplest form, the net elastic term for A and B blocks reads

$$\frac{F_A + F_B}{k_B T} \sim \frac{F_{el}}{k_B T} = \frac{3L_A^2}{2N_A a^2} + \frac{3L_B^2}{2N_B a^2} \quad (A.3)$$

More detailed considerations^{56,81} accounting for the nonuniform extension of blocks along their contours and for the location of block ends (one grafted at the interface and another one somewhere at the admissible distance within the brush) also yield $F_{el} = O(L_A^2 L_B^2)$, yet with somewhat different numerical coefficients and logarithmic corrections, either for the flat or spherical geometry of the interface.

As was mentioned above, the fraction of unreacted macromonomers within the copolymer layer is small and it

can be completely neglected (the so-called “dry brush approximation”) in order to express the layer widths L_A and L_B through the copolymer coverage n . In that case, the incompressibility condition for A (inner) and B (outer) layers covering a spherical droplet of radius R has the form

$$n = \frac{L_A \rho_0}{N_A a^3} \left(1 - \frac{L_A}{R} + \frac{L_A^2}{3R^2} \right) = \frac{L_B \rho_0}{N_B a^3} \left(1 + \frac{L_B}{R} + \frac{L_B^2}{3R^2} \right) \quad (\text{A.4})$$

where it is taken into account that a DPD liquid is ρ_0 times more dense than a usual melt. Introducing dimensionless parameters $\alpha = N_A/(N_A + N_B)$ and $\lambda = 3n(N_A + N_B)a^3/(\rho_0 R)$, we find from eq A.4 $L_A = R(1 - (1 - \alpha\lambda)^{1/3})$, $L_B = R((1 + (1 - \alpha)\lambda)^{1/3} - 1)$ and by substituting L_A and L_B into eq A.3 finally get eq 4 that determines the function $F_{\text{el}}(n)$.

By inserting eq A.2 into eq A.1 and replacing $F_A + F_B$ with F_{el} in the leading order, we can rewrite eq 1 in the form of a closed equation for $n(t)$

$$\frac{dn}{dt} = k_B \rho_A^0 \rho_B^0 \exp\left(-\frac{F_{\text{el}}(n)}{k_B T}\right) \quad (\text{A.5})$$

whose asymptotic solution at $F_{\text{el}} \gg k_B T$ is given by eq 3 in the main text.

AUTHOR INFORMATION

Corresponding Author

*E-mail: (Y.V.K.) yar@ips.ac.ru.

Notes

The authors declare no competing financial interest.

ACKNOWLEDGMENTS

The work was supported by the Russian Foundation for Basic Research (Project 12-03-00817a). We thank A. A. Gavrilov for the parallel realization of the DPD code. We are also grateful for the opportunity to use computational cluster Chebyshev at the Moscow State University.

REFERENCES

- (1) *Polymer Blends*, Paul, D. R., Bucknall, C. B., Ed.; Wiley: New York, 2000.
- (2) Koning, C.; Van Duin, M.; Pagnoulle, C.; Jerome, R. *Prog. Polym. Sci.* **1998**, 23, 707.
- (3) Litmanovich, A. D.; Platé, N. A.; Kudryavtsev, Y. V. *Prog. Polym. Sci.* **2002**, 27, 915.
- (4) Macosko, C. W.; Jeon, H. K.; Hoye, T. R. *Prog. Polym. Sci.* **2005**, 30, 939.
- (5) Jiang, G. J.; Wu, H.; Guo, S. Y. *Polym. Eng. Sci.* **2010**, 50, 2273.
- (6) Koulic, C.; Jerome, R. *Macromolecules* **2004**, 37, 3459.
- (7) Ruzette, A. V.; Leibler, L. *Nat. Mater.* **2005**, 4, 19.
- (8) Dong, W.; Jiang, F.; Zhao, L.; You, J.; Cao, X.; Li, Y. *ACS Appl. Mater. Interfaces* **2012**, 4, 3667.
- (9) Guo, Q.; Liu, J.; Chen, L.; Wang, K. *Polymer* **2008**, 49, 1737.
- (10) Yu, R.; Zheng, S.; Li, X.; Wang, J. *Macromolecules* **2012**, 45, 9155.
- (11) Xanthos, M., Ed. *Reactive extrusion*; Hanser Publ: Munich, Germany, 1992.
- (12) Kramer, E. J. *Isr. J. Chem.* **1995**, 35, 49.
- (13) Fredrickson, G. H. *Phys. Rev. Lett.* **1996**, 76, 3440.
- (14) O’Shaughnessy, B.; Sawhney, U. *Phys. Rev. Lett.* **1996**, 76, 3444.
- (15) O’Shaughnessy, B.; Sawhney, U. *Macromolecules* **1996**, 29, 7230.
- (16) Fredrickson, G. H.; Milner, S. T. *Macromolecules* **1996**, 29, 7386.
- (17) O’Shaughnessy, B.; Vavylonis, D. *Europhys. Lett.* **1999**, 45, 638.
- (18) O’Shaughnessy, B.; Vavylonis, D. *Eur. Phys. J. E.* **2000**, 1, 159.
- (19) Oyama, H. T.; Inoue, T. *Macromolecules* **2001**, 34, 3331.
- (20) Yeung, Ch.; Herrmann, K. A. *Macromolecules* **2003**, 36, 229.
- (21) Müller, M. *Macromolecules* **1997**, 30, 6353.
- (22) Yang, Y.; Char, K. *Macromol. Theory Simul.* **2001**, 10, 565.
- (23) John, A.; Nagel, J.; Heinrich, G. *Macromol. Theory Simul.* **2007**, 16, 430.
- (24) Cheng, M. H.; Balazs, A. C.; Yeung, Ch.; Ginzburg, V. V. *J. Chem. Phys.* **2003**, 118, 9044.
- (25) Berezkin, A. V.; Kudryavtsev, Y. V. *Macromolecules* **2011**, 44, 112.
- (26) Guseva, D. V.; Kudryavtsev, Y. V.; Berezkin, A. V. *J. Chem. Phys.* **2011**, 135, 204904.
- (27) Berezkin, A. V.; Guseva, D. V.; Kudryavtsev, Y. V. *Macromolecules* **2012**, 45, 8910.
- (28) Schulze, J. S.; Cernohous, J. J.; Hirao, A.; Lodge, T. P.; Macosko, C. W. *Macromolecules* **2000**, 33, 1191.
- (29) Schulze, J. S.; Moon, B.; Lodge, T. P.; Macosko, C. W. *Macromolecules* **2001**, 34, 200.
- (30) Jiao, J.; Kramer, E. J.; de Vos, S.; Möller, M.; Koning, C. *Macromolecules* **1999**, 32, 6261.
- (31) Oyama, H. T.; Ougizawa, T.; Inoue, T.; Weber, M.; Tamaru, K. *Macromolecules* **2001**, 34, 7017.
- (32) Jeon, H. K.; Macosko, C. W.; Moon, B.; Hoye, T. R.; Yin, Z. *Macromolecules* **2004**, 37, 2563.
- (33) Kim, H. Y.; Jeong, U.; Kim, J. K. *Macromolecules* **2003**, 36, 1594.
- (34) Yin, Z.; Koulic, C.; Pagnoulle, C.; Jérôme, R. *Langmuir* **2003**, 19, 453.
- (35) Zhang, J.; Lodge, T. P.; Macosko, C. W. *Macromolecules* **2005**, 38, 6586.
- (36) Yu, X.; Wu, Y.; Li, B.; Han, Y. *Polymer* **2005**, 46, 3337.
- (37) Kim, B. J.; Kang, H.; Char, K.; Katsov, K.; Fredrickson, G. H.; Kramer, E. J. *Macromolecules* **2005**, 38, 6106.
- (38) Harton, S. E.; Stevie, F. A.; Spontak, R. J.; Koga, T.; Rafailovich, M. H.; Sokolov, J. C.; Ade, H. *Polymer* **2005**, 46, 10173.
- (39) Kim, B. J.; Fredrickson, G. H.; Kramer, E. J. *Macromolecules* **2007**, 40, 3686.
- (40) Lamnawar, K.; Baudouin, A.; Maazouz, A. *Eur. Polym. J.* **2010**, 46, 1604.
- (41) Wang, D.; Fujinami, S.; Liu, H.; Nakajima, K.; Nishi, T. *Macromolecules* **2010**, 43, 5521.
- (42) Lyu, S. P.; Cernohous, J. J.; Bates, F. S.; Macosko, C. W. *Macromolecules* **1999**, 32, 106.
- (43) Bhadane, P. A.; Tsou, A. H.; Cheng, J.; Favis, B. D. *Macromolecules* **2008**, 41, 7549.
- (44) Yin, Z.; Koulic, C.; Jeon, H. K.; Pagnoulle, C.; Macosko, C. W.; Jérôme, R. *Macromolecules* **2002**, 35, 8917.
- (45) Hoogerbrugge, P. J.; Koelman, J. M. V. A. *Europhys. Lett.* **1992**, 19, 155.
- (46) Koelman, J. M. V. A.; Hoogerbrugge, P. J. *Europhys. Lett.* **1993**, 21, 363.
- (47) Espanol, P.; Warren, P. B. *Europhys. Lett.* **1995**, 30, 191.
- (48) Groot, R. D.; Warren, P. B. *J. Chem. Phys.* **1997**, 107, 4423.
- (49) Groot, R. D.; Madden, T. J. *J. Chem. Phys.* **1998**, 108, 8713.
- (50) Qian, H. J.; Lu, Z. Y.; Chen, L. J.; Li, Z. S.; Sun, C. C. *Macromolecules* **2005**, 38, 1395.
- (51) Feng, J.; Liu, H.; Hu, Y. *Macromol. Theory Simul.* **2006**, 15, 674.
- (52) Khokhlov, A. R.; Khalatur, P. G. *Chem. Phys. Lett.* **2008**, 461, 58.
- (53) Zhao, Y.; Liu, Y. T.; Lu, Z. Y.; Sun, C. C. *Polymer* **2008**, 49, 4899.
- (54) Li, X.; Pivkin, I. V.; Liang, H.; Karniadakis, G. E. *Macromolecules* **2009**, 42, 3195.
- (55) Wang, H.; Liu, Y. T.; Qian, H. J.; Lu, Z. Y. *Polymer* **2011**, 52, 2094.
- (56) Semenov, A. N. *Sov. Phys. JETP* **1985**, 61, 733.
- (57) Besold, G.; Vattulainen, I.; Karttunen, M.; Polson, J. M. *Phys. Rev. E* **2000**, 62, R7611.
- (58) Akkermans, R. L. C.; Toxvaerd, S.; Briels, W. J. *J. Chem. Phys.* **1998**, 109, 2929.

- (59) Khokhlov, A. R.; Berezkin, A. V.; Khalatur, P. G. *J. Polym. Sci. A, Polym. Chem.* **2004**, *42*, 5339.
- (60) Liu, H.; Qian, H. J.; Zhao, Y.; Lu, Z. Y. *J. Chem. Phys.* **2007**, *127*, 144903.
- (61) Gavrilov, A. A.; Guseva, D. V.; Kudryavtsev, Y. V.; Khalatur, P. G.; Chertovich, A. V. *Polym. Sci. Ser. A* **2011**, *53*, 1207.
- (62) Berezkin, A. V.; Solov'ev, M. A.; Khalatur, P. G.; Khokhlov, A. R. *J. Chem. Phys.* **2004**, *121*, 6011.
- (63) Leibler, L. *Macromol. Chem., Macromol. Symp.* **1988**, *16*, 1.
- (64) Gohy, J. F. *Adv. Polym. Sci.* **2005**, *190*, 65.
- (65) Discher, D. E.; Eisenberg, A. *Science* **2002**, *297*, 967.
- (66) Rodriguez-Garcia, R.; Mell, M.; Lopez-Montero, I.; Netzel, J.; Hellweg, T.; Monroy, F. *Soft Matter* **2011**, *7*, 1532.
- (67) Meng, F.; Zhong, Z.; Feijen, J. *Biomacromolecules* **2009**, *10*, 197.
- (68) Shen, H.; Eisenberg, A. *J. Phys. Chem. B* **1999**, *103*, 9473.
- (69) Riegel, I. C.; Eisenberg, A.; Petzhold, C. L.; Samios, D. *Langmuir* **2002**, *18*, 3358.
- (70) Jain, S.; Bates, F. S. *Science* **2003**, *300*, 460.
- (71) Zhu, J.; Liao, Y.; Jiang, W. *Langmuir* **2004**, *20*, 3809.
- (72) Talingting, M. R.; Munk, P.; Webber, S. E. *Macromolecules* **1999**, *32*, 1593.
- (73) Cameron, N. S.; Corbierre, M. K.; Eisenberg, A. *Can. J. Chem.* **1999**, *77*, 1311.
- (74) Kinning, D. J.; Winey, K. I.; Thomas, E. L. *Macromolecules* **1988**, *21*, 3502.
- (75) Wyman, I.; Njikang, G.; Liu, G. *Prog. Polym. Sci.* **2011**, *36*, 1152.
- (76) Ohta, T.; Nonomura, M. *Prog. Colloid Polym. Sci.* **1997**, *106*, 127.
- (77) Zhu, J.; Hayward, R. C. *J. Am. Chem. Soc.* **2008**, *130*, 7496.
- (78) Zhu, J.; Hayward, R. C. *J. Colloid Interface Sci.* **2012**, *365*, 275.
- (79) Blanazs, A.; Madsen, J.; Battaglia, G.; Ryan, A. J.; Armes, S. P. *J. Am. Chem. Soc.* **2011**, *133*, 16581.
- (80) Charleux, B.; Delaittre, G.; Rieger, J.; D'Agosto, F. *Macromolecules* **2012**, *45*, 6753.
- (81) Zhulina, E. B.; Borisov, O. V. *Macromolecules* **2012**, *45*, 4429.